

KaLDeX: Kalman Filter based Linear Deformable Cross Attention for Retinal Vessel Segmentation

Zhihao Zhao^{a,b}, Shahrooz Faghihroohi^a, Yinzheng Zhao^b, Junjie Yang^{a,b}, Shipeng Zhong^c, Kai Huang^c, Nassir Navab^a, Boyang Li^{c,*}, M. Ali Nasseri^{a,b,*}

^aTechnical University of Munich, Arcisstrasse 21, Munich, 80333, , Germany

^bKlinik und Poliklinik für Augenheilkunde (TUM), IsmaningerStr. 22, Munich, 81675, , Germany

^cSun Yat-Sen University, Xingang Xi Road 135, Guangzhou, 510275, , China

Abstract

Background and Objective: In the realm of ophthalmic imaging, accurate vascular segmentation is paramount for diagnosing and managing various eye diseases. Contemporary deep learning-based vascular segmentation models rival human accuracy but still face substantial challenges in accurately segmenting minuscule blood vessels in neural network applications. Due to the necessity of multiple downsampling operations in the CNN models, fine details from high-resolution images are inevitably lost. The objective of this study is to design a structure to capture the delicate and small blood vessels.

Methods: To address these issues, we propose a novel network (**KaLDeX**) for vascular segmentation leveraging a Kalman filter based linear deformable cross attention (LDCA) module, integrated within a UNet++ framework. Our approach is based on two key components: Kalman filter (KF) based linear deformable convolution (LD) and cross-attention (CA) modules. The LD module is designed to adaptively adjust the focus on thin vessels that might be overlooked in standard convolution. The CA module improves the global understanding of vascular structures by aggregating the detailed features from the LD module with the high level features from the UNet++ architecture. Finally, we adopt a topological loss function based on persistent homology to constrain the topological continuity of the segmentation.

Results: The proposed method is evaluated on retinal fundus image datasets (DRIVE, CHASE_BD1, and STARE) as well as the 3mm and 6mm of the OCTA-500 dataset, achieving an average accuracy (ACC) of 97.25%, 97.77%, 97.85%, 98.89%, and 98.21%, respectively.

Conclusions: Empirical evidence shows that our method outperforms the current best models on different vessel segmentation datasets. Our source code is available at: <https://github.com/AIEyeSystem/KaLDeX>.

Keywords:

Retinal Vessel Segmentation,
Linear Deformable,
Cross-Attention,
Kalman Filter

1. Introduction

The accurate segmentation of the retinal vasculature is essential in diagnosing and treating a myriad of eye diseases [1, 2]. The retina, a crucial component of the human eye, provides essential insights into systemic health conditions, such as diabetes and hypertension, which manifest in vascular changes. In the clinical setting, ophthalmologists are capable of diagnosing ocular diseases not only by evaluating parameters such as the diameter of blood vessels and branching coefficients but also by formulating surgical plans based on the structure and location of these vessels [3, 4, 5]. Traditionally, retinal segmentation has been performed manually by clinicians, a process that is

not only time-consuming but also prone to errors due to the intricate nature of the retinal vasculature [6]. This complexity underscores the necessity for a reliable, computer-assisted automated segmentation approach, which can offer more precision and efficiency in clinical diagnostics and research.

Advancements in machine learning and deep learning have spurred a multitude of methodologies for retinal segmentation [7, 8, 9]. Early approaches included handcrafted features and filtering-based methods. However, these techniques often lacked flexibility and robustness, particularly in diverse and challenging imaging conditions [10, 11, 12]. The emergence of UNet-based deep learning architectures marked a significant milestone in the field, establishing new standards for accuracy and efficiency in retinal segmentation [13, 14, 15]. These models, known for their deep convolutional networks, brought about a remarkable improvement in performance, showcasing an ability to achieve accuracy levels on par with human experts. How-

*Corresponding author: Boyang Li, M. Ali Nasseri.

Email address: liby83@mail.sysu.edu.cn,

ali.nasseri@mri.tum.de (M. Ali Nasseri)

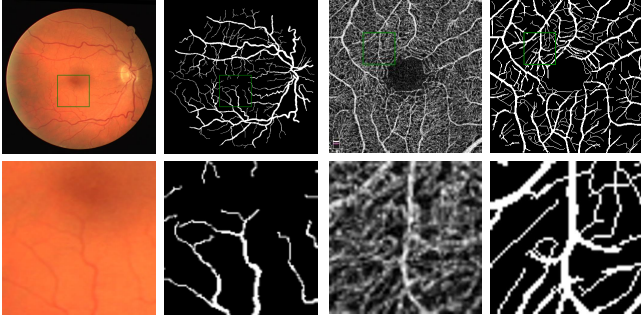


Figure 1: The first row shows the ophthalmic images and their segmentation masks. The second row represents the ROI (region of interest) areas from the first row (in green). The ROI indicates the thin vascular structures that are difficult to recognize.

ever, due to the necessity of multiple downsampling operations in the U-Net model, fine details from high-resolution images are inevitably lost [16, 17]. This is particularly problematic for retinal vessel segmentation, especially resembling the small vascular structures illustrated in Fig. 1. Despite the incorporation of skip connection layers to partially compensate for this loss, the issue of significant information loss persists, particularly for delicate and small blood vessels.

To mitigate the loss of information caused by downsampling, U-Net++ [15] employs a strategy involving multiple nested skip connections to assist in capturing feature information from different layers. However, for minuscule vascular structures, conventional convolutional methods struggle to accurately represent the spatial positioning information of linear objects. Deformable convolutions, through dynamically adjusting the convolutional field of view, can perceive the spatial contour information of objects [18]. Yet, when it comes to specific structures like blood vessels, the network architecture faces challenges in capturing their curve characteristics [19]. This highlights the ongoing need for advancements in convolutional techniques and network architectures to better understand and process the unique properties of such intricate structures.

To address these limitations, we introduce a novel approach **KaLDeX**, that enhances retinal vessel segmentation accuracy by leveraging a Kalman filter based linear deformable cross attention mechanism. Our network includes two innovative modules: a Kalman filter (KF) based linear deformable convolution module (LD) and a cross-attention module (CA). The LD module is inspired by the deformable convolution networks (DCNs) [18] and dynamic snake convolution network (DSCNet) [20] structures. In DSCNet, a two-dimensional convolution is unfolded, and coordinates are iteratively accumulated to deform the convolution for capturing tubular structures. However, this iterative approach may lead to the accumulation of errors. This paper addresses this issue by employing the KF module to mitigate errors during the iterative process. Moreover, to more precisely capture the structural information of small vessels, we aggregate the vascular field of view perceived by the LD module with the extensive vascular contextual information obtained from up-sampling and down-sampling in the U-Net++ [15] structure using the CA module. By aggregating the de-

tailed features captured by LD module with the global information obtained through the feature map in U-Net++, the network gains a more comprehensive understanding of the vascular network. Furthermore, in order to ensure the continuity and topological structure of vascular structures, we employ the Centerline Dice (clDice) [21] loss function and the optimized topological [22] loss function to reveal the topological continuity of the segmentation structure. This approach not only enhances the fidelity of vessel segmentation but also preserves the geometric integrity of vascular structure. Our contributions can be summarized as follows:

1. We propose a Kalman filter based linear deformable module suitable for vascular segmentation in ophthalmic images, which enables the convolutional field of view to focus more on the vascular regions.
2. We aggregate feature maps captured by LD modules with the global information obtained through U-Net++ to enhance the network’s ability to discern small vascular structures.
3. We integrate the clDice loss and Optimized topological loss to constrain the overall connectivity and geometric integrity of vascular structure.

Empirical evidence demonstrates that our method surpasses the capabilities of the current best models in retinal vessel segmentation. Our source code is available at <https://github.com/AIEyeSystem/KaLDeX>

2. Related Work

2.1. U-Net in Retinal Vessel Segmentation

The U-Net network [13], initially introduced for biomedical image segmentation, has significantly influenced the field of retinal vessel segmentation [23, 24]. Its unique U-shaped design combines a contracting path to capture context with a symmetric expanding path for precise localization, proving especially effective in dealing with the complex structures of the retina.

Since the inception of U-Net, lots of U-Net variants have been developed to enhance its performance further [25, 26, 27]. To enable the network to achieve greater complexity and depth, (author?) [28] proposed ResUNet, which incorporates residual connections into the U-Net framework. ResUNet eases the training of deeper networks by allowing gradients to flow more effectively through the architecture. This modification is particularly useful for more complex segmentation tasks, where deeper models may be required to capture intricate patterns and structures. When networks become excessively large and deep, they are prone to overfitting [29], where they learn to memorize training data rather than generalize well to unseen data. SD-UNet [30] enhances the regularization of U-Net by departing from traditional convolutional layer dropout mechanisms and instead employing structured dropout [31]. This departure significantly mitigates overfitting issues inherent in U-Net architectures, thereby bolstering the end-to-end capability of vessel

segmentation. The U-Net++ [15] introduces nested, dense skip pathways, improving segmentation accuracy by reducing the semantic gap between the encoder and decoder feature maps. FR-UNet [32] is a notable deep learning architecture tailored for retinal vessel and coronary angiograph segmentation, featuring a distinctive full-resolution approach augmented by a dual-threshold iteration technique for enhanced accuracy. However, U-Net++ and FR-UNet are not specifically designed to capture tubular structures, so there is still a loss of small vessels in the curve characterization of the captured vessels.

2.2. Deformable Convolution

Deformable convolution adds a dynamic adjustment to the spatial sampling locations in the standard convolutional operation [18]. This modification allows the network to adaptively change its receptive field based on the input features, making it more effective in handling geometric deformations and variations in object shapes [33, 34]. In the context of medical image analysis, this capability is particularly valuable for capturing the intricate and varied structures of retinal vessels [35, 19].

The deformable convolutional blocks are designed to model retinal vessels of various shapes and sizes by learning local, dense, and adaptive receptive fields by (author?) [19] in the DUNet architecture. This is achieved by integrating low-level features with high-level features, where both the receptive field and the sampling locations are adaptively trained based on the scale and shape of the vessels, facilitating precise segmentation. DCU-Net [36] also leverages U-Net as a submodule, which is then cascaded to deepen the network. To ensure effective information exchange between different submodules, a Residual Channel Attention Module (RCAM) is proposed to connect the U-Net subnetworks. This ensures that features from the primary and secondary U-Net subnetworks can be effectively integrated, significantly enhancing the capability to model vascular deformations.

2.3. Attention Mechanism in Segmentation

The integration of attention mechanisms [37, 38] into deep learning models for retinal vessel segmentation has marked a significant evolution in the precision and efficiency of these models [39, 40, 41]. Recent works have demonstrated the efficacy of attention-based approaches in enhancing model sensitivity to relevant features while suppressing irrelevant information, leading to more accurate segmentation outcomes [42, 43, 44, 45]. For instance, SA-UNet [46] integrates attention mechanisms, allowing the model to focus on relevant features, thus distinguishing between retinal vessels and background noise more effectively. CCS-UNet [47] enhances cross-channel weight distribution by combining soft attention, effectively aggregating contextual information in vascular images. The attention mechanism within skip connections aids in strengthening feature integration across layers [48, 49, 50], thus alleviating degradation of pertinent information. It facilitates cross-channel information retrieval and enhances localization of regions of interest, ultimately improving the identification of vascular structures.

3. Methods

3.1. Structure Overview

Fig. 2(a) represents the overall structure of our **KaLDeX** model. The network utilizes UNet++ as our foundational backbone, comprising convolutional layers, up-sampling and down-sampling layers, along with our Kalman filter based linear deformable cross attention (LDCA) module. Fig. 2(b) showcases our proposed LDCA module, which primarily consists of two sub-modules: Kalman filter (KF) based Linear Deformable (LD) Convolution and Cross-Attention (CA). Fig. 2(b₁) is the LD sub-module, which is primarily focused on capturing vascular structure information more effectively through deformable convolution. Simultaneously, we employ KF to reduce the accumulation of errors in convolutional kernel coordinate offsets during the execution of deformable convolutions. This optimization aims to obtain a feature map from linear deformable convolutions that closely represents the vascular structure in the acquired field of view. Fig. 2(b₂) illustrates that the CA submodule enhances the model’s ability to discern small vessels and understand the vascular structure context by aggregating the output feature map of LD with the feature maps obtained from up-sampling and down-sampling in UNet++.

3.2. Model input

To accommodate inputs of varying shapes and sizes, we initially preprocess each image into multiple $W \times W$ patches with a stride of S , with each patch independently fed into the network. In the paper, we set $W = 48$ and $S = 24$. The model’s modules serve three primary functions: 1) feature extraction from inputs via standard 3×3 convolutions with padding, 2) progressive downsampling of inputs into a more compressed space, and 3) upsampling of inputs into the semantic segmentation space. As illustrated in Fig. 2(a), following the UNet++ architecture, the network enhances feature fusion between the encoder (down-sampling) and decoder (upsampling) segments through nested skip connections. Here, blue feature maps represent standard 3×3 convolutions with padding, maintaining the same shape after convolution as the original feature maps. The white feature maps denote the results of downsampling, halving the size of the input feature maps.

3.3. Kalman Filter based Linear Deformable Convolution

Our linear deformable convolution (LD) structure is inspired by deformable convolution networks (DCNs) [18] and dynamic snake convolution networks (DSCNet) [20]. DCNs adjust their convolutional field of view by predicting an offset, thus extending the convolutional view to regions suitable for the object. DSCNet advances this concept by further expanding the convolution to fit tubular areas. It calculates the entire convolutional field of view iteratively by predicting the deviation between the current and previous positions. Although this method effectively maintains the continuity of linear structures, it also results in the accumulation of prediction errors. To address this issue, we utilize a Kalman filter-based approach to reduce the error accumulation in the calculation of the linear convolutional field of view’s position.

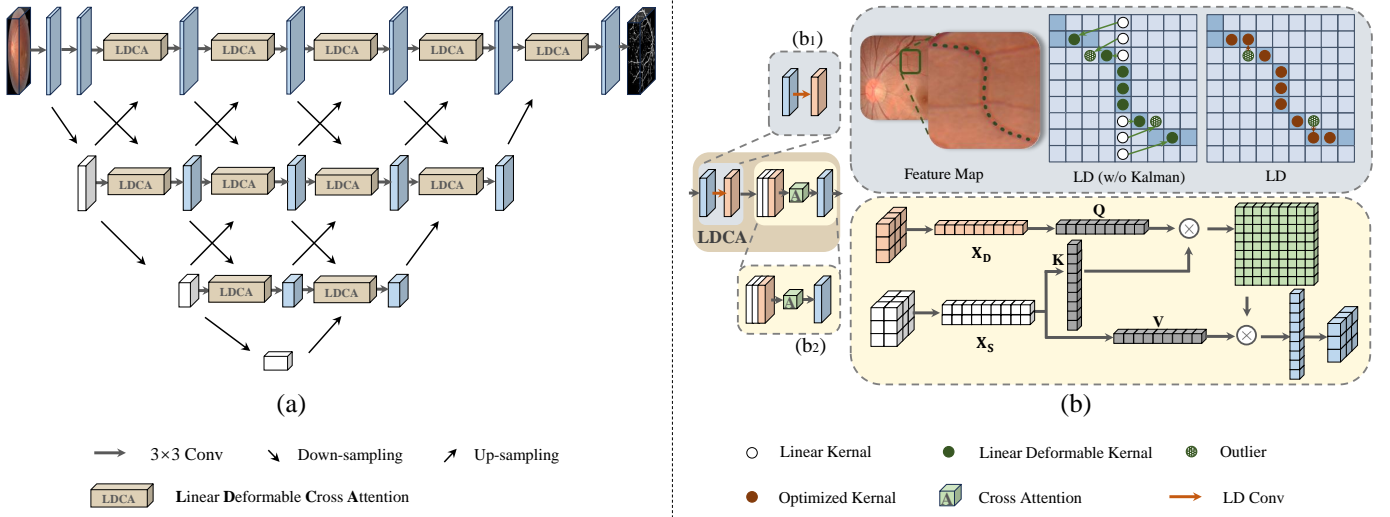


Figure 2: Overview of our proposed **KaLDeX**. (a) is the overall framework of our proposed structure. (b) showcases the key module (LDCA), which primarily consists of two sub-modules: LD(b_1) and CA(b_2). LD is primarily focused on capturing vascular structures through deformable convolutions and optimizing the coordinates of deformable convolutions using KF. CA aggregates the output feature maps of LD with the feature maps obtained from up-sampling and down-sampling in the network.

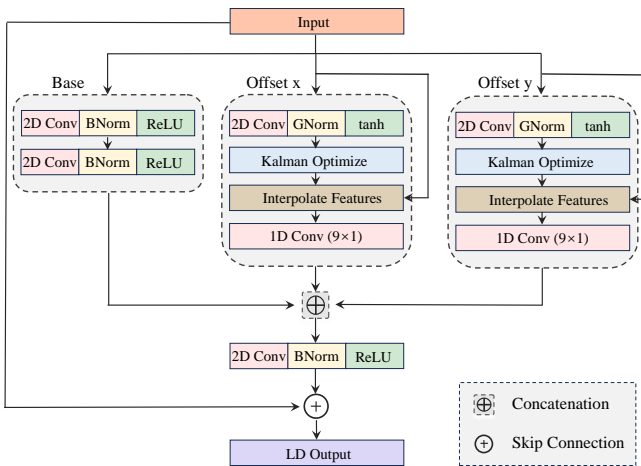


Figure 3: LD is primarily focused on capturing vascular structures through LD module and optimizing the coordinates of convolutions using KF.

The detailed architecture of our Linear Deformable (LD) module is depicted in Fig. 3, which begins by receiving a feature map as input. This feature map is then directed to three distinct modules: a base convolution module, a horizontal deformable convolution module (Offset x), and a vertical deformable convolution module (Offset y). The base convolution module employs two successive 3×3 convolutions with padding to further extract features of the same size while increasing the channel count of the feature map to capture more detailed information. The linear deformable module encompasses an offset convolution, a Kalman filter optimization module, a feature interpolation module, and a linear convolution module. The principles behind the horizontal and vertical linear deformable modules are similar, differing primarily in the computation of offsets—where one calculates only the x offsets and the other

only the y offsets. Subsequently, during linear convolution, the lateral module utilizes a convolution of dimensions $(1 \times \text{Kernel})$, whereas the vertical module employs a convolution of dimensions $(\text{Kernel} \times 1)$.

The main task of the offset convolution module is to learn the deformation offsets required for the convolution kernel. As illustrated in Fig. 4(a), the learned offsets can alter the field of view of the convolution kernel, from its initial field represented by the white circle, to a shifted field more aligned with the vascular structure. As shown in Fig. 4(b), the KF module corrects erroneous convolutional fields of view to a reasonable position based on historical information about the convolutional kernel coordinates. Subsequently, a linear convolution captures the shifted field of view, enabling the entire module to adaptively extract features from the vascular regions through deformable linear convolution.

In our paper, the linear convolutions employed are one-dimensional linear convolution kernels sized 9×1 and 1×9 , respectively. In the following part of this paper, we will only explain in detail how to optimize the coordinates for the x offsets; the vertical coordinates for y offsets are similar to the x offsets. Each convolution kernel is represented as $\text{Ker} = (x_{i \pm c})$, where $c = 0, 1, 2, 3, 4$. DSCNet utilizes a learnable offset δ to predict the deviation in coordinates of the deformed convolution kernel $x_i = x_{i-1} + \delta_i$. Each new coordinate is the sum of the previous coordinate and the predicted deviation, resulting in cumulative errors. The Kalman filter is a highly effective method for reducing cumulative errors when predicting future values by weighting the current value and previous values [51]. The optimization of linear deformable convolution by Kalman filtering is achieved by assigning a weight K to the convolution kernel offset δ_i . For a 1×9 convolution kernel, we start from the center of the kernel x_0 , and then iteratively compute $x_i = (1 - K_i)x_{i-1} + K_i(x_{i-1} + \delta_i)$ ($i = 1, 2, 3, 4$) using Kalman

update Equation 1. Here, K_i denotes the Kalman gain, computed iteratively based on Equation 1, where p_i signifies the estimate covariance of the error between estimated coordinates and predicted coordinates from the LD module, and r is a hyperparameter related to measurement errors from neural network outputs. The hyperparameter r is empirically set to 0.01. The initial values of p_0 and x_0 are set to 1 and 0 respectively. These parameters will be updated iteratively during the process.

$$\begin{cases} K_i = \frac{p_{i-1}}{p_{i-1}+r} \\ x_i = (1 - K_i)x_{i-1} + K_i(x_{i-1} + \delta_i) = x_{i-1} + K_i\delta_i \\ p_i = (1 - K_i)p_{i-1} \end{cases} \quad (1)$$

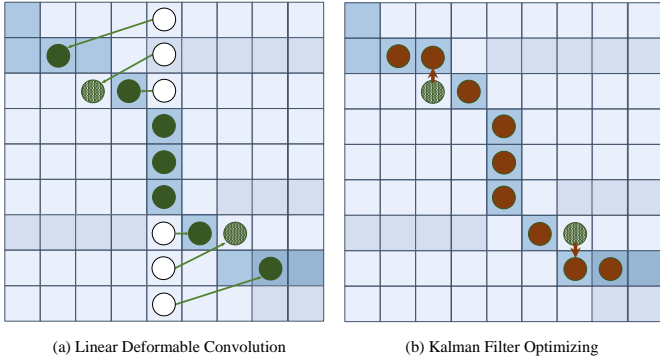


Figure 4: In figure (a), the gray background illustrates the vascular area, while white circles symbolize standard one-dimensional convolution. Green circles represent the positions of the field of view following linear deformable convolution. In figure (b), brown circles denote points that have been optimized using Kalman filter.

3.4. Cross Attention Aggregation Module

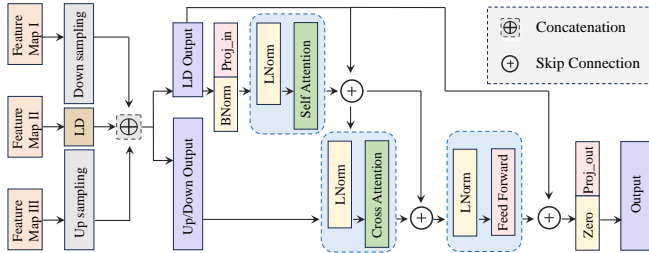


Figure 5: CA aggregates the output feature maps of LD with the feature maps obtained from up-sampling and down-sampling in the network.

Inspired by the advantage that cross-attention mechanisms can capture the associative information between different positions within two input sequences, the CA module in our work is utilized to aggregate the vascular detail information obtained from the LD module and the vascular contextual features derived from up-sampling and down-sampling in UNet++. As illustrated in Fig. 2(b₂) in the color figure, the feature maps obtained by regular convolution are represented in blue, the feature maps resulting from the LD module are represented in orange, and the feature maps in white represent the results from the up-sampling and down-sampling in UNet++. Initially, we

need to flatten the feature maps into one dimension. Then, the result X_D of the LD module is transformed into Q matrix through a linear connection layer W_Q , while the up-sampling and down-sampling results X_S of UNet++ are transformed into K and V matrices through W_K and W_V , respectively. The Q and K matrices are multiplied to create an attention map. This attention map is multiplied with the V matrix to yield the aggregated result. Finally, the output is reshaped to match the shape of the input image. Overall, the entire aggregation process can be defined by Equation 2, where d_k is the dimension of K .

$$CA(X_D, X_S) = \text{softmax}\left(\frac{QK^T}{\sqrt{d_k}}\right)V \quad (2)$$

$$Q = W_Q X_D, K = W_K X_S, V = W_V X_S$$

3.5. Loss Function

In the segmentation of vascular structures, besides focusing on small vascular details, the overall continuity in the vascular space is also crucial. To maintain the connectivity in the segmentation results, we combine the cDice loss [21] based on structure similarity along with the cross-entropy loss function to form our new loss. The cDice loss is defined according to Equation 3, where V_L is the ground truth of vascular segmentation, V_P is the predicted result, S_L is the skeleton extracted from the ground truth, and S_P is the skeleton extracted from the predicted result. The topological accuracy $T\text{prec}(S_P, V_L)$ and topological sensitivity $T\text{sens}(S_L, V_P)$ can be defined accordingly.

$$\begin{aligned} T\text{prec}(S_P, V_L) &= \frac{|S_P \cap V_L|}{|S_P|} \\ T\text{sens}(S_L, V_P) &= \frac{|S_L \cap V_P|}{|S_L|} \\ \text{cDice}(V_P, V_L) &= 2 \times \frac{T\text{prec}(S_P, V_L) \times T\text{sens}(S_L, V_P)}{T\text{prec}(S_P, V_L) + T\text{sens}(S_L, V_P)} \end{aligned} \quad (3)$$

Finally, the weighted sum of cDice and cross-entropy loss function is employed as the loss function:

$$\mathcal{L}_{oss} = \alpha(1 - \text{cDice}) + (1 - \alpha)\mathcal{L}_{BCE} \quad (4)$$

Since cDice represents similarity, we optimize $1 - \text{cDice}$ in the loss function. α is empirically set to 0.4.

3.6. Fine-tuning Using Topological Loss.

To further enhance the overall topological continuity of the segmentation results, we propose a modified persistent homology-based topological loss based on [20, 52] to measure the topological error between the persistence diagrams of the predictions and the ground truth. Due to the computationally intensive nature of topological analysis, we did not directly incorporate topological loss during the initial training phase. Instead, we chose to refine the segmentation results using topological loss after the segmentation model had been fully trained. Topological Data Analysis (TDA) [53] infers relevant topological and geometric features from complex data. We use the TopologyLayer tool [54] for persistent homology in topological analysis. By employing a mechanism known as simplicial filtration, we construct the high-dimensional relationships

of the vascular structures in the input image to generate persistence barcodes, or persistence diagrams (PD). The generation of a persistence diagram can be defined as $PD = dgm()$, where 0-dimensional features are connected components. The persistence diagram of the segmentation result is defined as $PD_S = dgm(S)$, and the persistence diagram of the ground truth is defined as $PD_{GT} = dgm(GT)$. We use the Hausdorff distance to measure the similarity between the segmentation results and the ground truth. However, the traditional Hausdorff distance is highly sensitive to outliers, and the segmentation results often contain a significant amount of noise. This sensitivity can severely affect the distance measurement between persistence diagrams (PD). Therefore, in Equation 5, we adopt a method of computing the Hausdorff distance using a weighted sum of the distances between all points.

$$d_H(PD_S, PD_{GT}) = \frac{1}{2} \left(\frac{\sum_{a \in PD_S} \min_{b \in PD_{GT}} \|a - b\|}{|PD_S|} + \frac{\sum_{b \in PD_{GT}} \min_{a \in PD_S} \|b - a\|}{|PD_{GT}|} \right) \quad (5)$$

Here, $|PD_S|$ and $|PD_{GT}|$ represent the number of points in the sets PD_S and PD_{GT} , respectively. The original Hausdorff distance considers only the farthest single point, making it highly sensitive to noise and outliers, as a single outlier far from the other points can significantly increase the Hausdorff distance. The modified Hausdorff distance, however, replaces the maximum distance in the original Hausdorff distance with the average distance from each point to the nearest point in the other set. This means that the impact of a single extreme value is distributed across all points, thereby reducing its contribution to the total distance. Since the topological loss is calculated for the point sets of each segmentation class separately, during the finetuning phase, the topological loss is represented as $\mathcal{L}_{OSS_{tp}} = \sum_0^N d_H$, where N denotes the number of categories of segmentation. For vascular segmentation, there is only one class (excluding the background), so $\mathcal{L}_{OSS_{tp}} = d_H$. We then combine the cross-entropy loss function and the topological loss function to form our finetuning phase loss function $\mathcal{L}_{OSS} = \mathcal{L}_{OSS_{tp}} + \mathcal{L}_{BCE} = H + \mathcal{L}_{BCE}$.

3.7. Inference Phase

During the inference phase, we employ the same strategy as in the training phase, segmenting the image into multiple $W \times W$ patches with a stride of $S = W/2$. Since stride is half the size of patches, there is overlap between patches. To ensure that the re-assembled image appears more natural and coherent, we assign weights to each pixel within a segmented image, starting from the center, based on the inverse of their distance, as described by Equation 6. When combining segmented patches from an image, these weights are used to decide the influence of each patch on the final combined output. Typically, patches that are centrally located are given more significance than those on the periphery, which helps in reducing artifacts at the edges and improving the smoothness of the transition between patches. This

weighting approach facilitates a more seamless integration of the results from two adjacent patches.

$$\begin{cases} WeightMap[i][j] = \frac{1}{\sqrt{(W/2 - i)^2 + (W/2 - j)^2 + 1}} \\ (0 \leq i < W, 0 \leq j < W) \end{cases} \quad (6)$$

4. Results

4.1. Setup Details

4.1.1. Datasets

Experiments are carried out on publicly available ophthalmic datasets. The **DRIVE** [55] dataset encompasses 40 retinal images with segmentation annotations; 33 images are devoid of diabetic retinopathy, and 7 demonstrate early mild symptoms. Captured at a resolution of 565×584 pixels using 8 bits per color channel, this dataset is divided into training and testing subsets, each containing 20 images. The **CHASE_DB1** [56] dataset, aimed at retinal vessel segmentation, comprises 28 color retina images (999×960 pixels) sourced from both eyes of 14 schoolchildren. These images undergo manual segmentation annotation by two independent experts, with the first expert’s annotation often accepted as the benchmark. Following established conventions, the first 20 images are designated for training and the remaining 8 for testing. The **STARE** [57] dataset includes 20 retinal fundus images, half of which display pathologies. In the absence of predefined divisions, it utilizes a 10-fold cross-validation strategy, assigning 18 images for training and the remainder for testing across ten iterations, thereby ensuring thorough evaluation and reliability. The **FIVES** dataset [58] is a significantly larger dataset, containing 800 retinal images (2048×2048 pixels) from 573 individuals; it has annotation consistency by 3 ophthalmologists and 24 medical staff. It comprises images from 200 normal eyes and 200 each from the AMD, DR, and GC categories. The **OCTA-500** [59] dataset comprises 500 OCTA projection images, including 300 images with a 6×6 mm field of view and 200 images with a 3mm×3mm field of view. Each image is accompanied by corresponding annotations. We utilize the last 50 images for testing for both datasets, while the remaining images are used for training.

For all datasets, we have not separately partitioned a validation set. Instead, we divide the images in the training set into multiple patches of size 48×48. Within all patches, we further split the data into a training set and a validation set in a 1:9 ratio.

4.1.2. Evaluation Metric.

We calculate the area under the ROC curve (AUC) between the segmentation results and the ground truth. Additionally, we systematically evaluate other segmentation metrics, including accuracy (Acc), sensitivity (Sen), specificity (Spe), F1 score or

DICE score, and Intersection over Union (IOU).

$$\begin{aligned}
 Acc &= \frac{TP + TN}{TP + TN + FP + FN} \\
 Sen &= \frac{TP}{TP + FN} \\
 Spe &= \frac{TN}{TN + FP} \\
 F1 = DICE &= \frac{2TP}{2TP + FP + FN} \\
 IOU &= \frac{TP}{TP + FP + FN}
 \end{aligned} \tag{7}$$

To evaluate the connectivity performance of the segmented vascular structures, we employed the cIDice metric to calculate the connectivity performance of our segmentation results. cIDice is calculated similar to cIDice loss in Section 3.5.

4.1.3. Experimental Settings.

Our experimental setup utilizes a single NVIDIA RTX A5000 GPU with 24GB memory and is implemented using PyTorch. The learning rate is initially set to $1e-4$, and for optimization, the Adam optimizer is employed with a weight decay of $1e-5$. During the training phase, preprocessing of images is conducted as follows: color images are converted to grayscale and uniformly normalized. Subsequently, a 48×48 sliding window with a stride of 24 is utilized to crop the training images. The dataset is trained for 10 epochs and then further fine-tuned using topological loss for 5 epochs. To mitigate overfitting, on-line data augmentation techniques such as horizontal and vertical flipping are employed, along with the addition of Gaussian noise using a 5×5 kernel.

4.2. Evaluation and Results

4.2.1. Results of Segmentation

In the experiment section, we presented a comprehensive evaluation of our proposed model’s performance in segmenting vascular map from medical imaging datasets, specifically focusing on fundus images and Optical Coherence Tomography Angiography (OCTA) datasets. The input to our model consisted of 48×48 pixel patches, which were carefully extracted from the original images to train the network effectively. These patches were meticulously reassembled back into their full size during the testing phase to ensure a thorough assessment and facilitate a direct comparison with the original image dimensions.

In this study, we conducted a comprehensive evaluation of our vascular segmentation experiments, benchmarking our approach against some of the most prominent methods in the field. We compared with models from the UNet family, including UNet [13], UNet++ [15] and FR-UNet [32], along with PVT-GCASCADE [60], which employ attention mechanisms, and SwinUNETRV2 [61] and TransUNet [62], which incorporate transformer architectures. Additionally, DUnet [19], which utilizes deformable convolutions, was also employed for benchmark testing. Fig. 6 showcases the segmentation results obtained from our model alongside those from existing conventional network architectures. This comparison is critical in

highlighting the strengths and potential areas of improvement for each method. A closer inspection of the cropped areas within the figure uncovers a significant insight: many of the fine and faint vascular structures, which are crucial for accurate diagnosis and are often present in fundus images, are consistently missed or inadequately captured by the conventional networks. These networks, while robust in many applications, lack the sensitivity and specificity required to detect the smallest of vessels, which are essential markers in the early diagnosis of various ocular diseases. On the contrary, our network showcases exceptional proficiency in identifying and segmenting small vessels, capturing intricate vascular details often overlooked by conventional methods. These results demonstrate the advantages of our network, which incorporates a cross-attention module to consolidate detailed features captured by the linear deformable convolution and the broader contextual information obtained through the up-sampling and down-sampling of the UNet++ architecture. This aggregation process proves essential for the network to attain a more comprehensive understanding of vascular structures, enabling the model to distinguish between closely situated vessels and other anatomical structures.

Furthermore, our evaluation encompasses a suite of metrics such as AUC, Acc, and the DICE coefficient, among others, to conduct a quantitative analysis that highlights the superior performance of our proposed model relative to competing methodologies. Table 1 provides a detailed quantitative comparison across various models on the DRIVE and CHASE_DB1 datasets, illustrating the effectiveness of our approach in the segmentation of vascular structures within fundus images. Similarly, Table 2 showcases comparative performance metrics on the STARE dataset, reinforcing our model’s adeptness in this domain. Both Table 1 and Table 2 are pivotal in underscoring the precision of our model in identifying vascular structures, an area of critical importance in fundus image analysis. Additionally, Table 3 delineates our model’s segmentation prowess on the OCTA dataset, further substantiating the versatility and robustness of our proposed structure across varied imaging modalities.

The empirical evidence presented in Tables 1 and 2 unequivocally demonstrates that our proposed model sets a new benchmark in accuracy (ACC) on the DRIVE, CHASEDB1, and STARE datasets, achieving scores of 97.25%, 97.77%, and 97.85%, respectively. These results are not only limited to accuracy but extend to other evaluative metrics as well, where our method exhibits commendable performance. Detailed insights into these achievements are systematically catalogued in the concluding rows of Tables 1 and 2.

In the context of the OCTA dataset, our analytical focus was primarily directed towards two metrics: ACC and the DICE coefficient. The outcomes, as depicted in Table 3, underscore our method’s unparalleled efficacy, marking it as the top-performing approach on both the OCTA_3mm and OCTA_6mm datasets with the highest recorded values for the mentioned metrics. These results not only highlight the methodological advancements embedded within our model but also its adaptability and effectiveness in addressing the complexities inherent in vascular structure segmentation across different datasets.

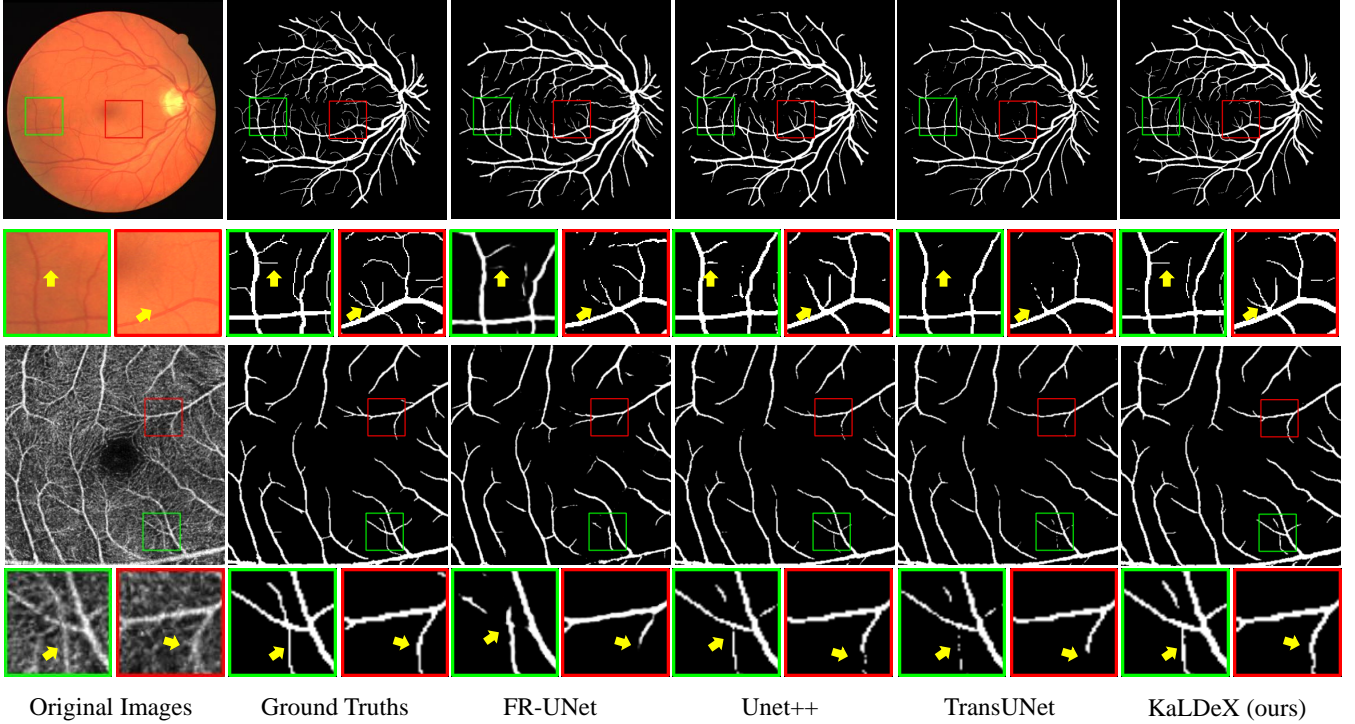


Figure 6: Visualization of segmentation results. The first and third rows depict the segmentation results of fundus images and OCTA, respectively, while the second and fourth rows display magnifications of the cropped regions.

4.2.2. Segmentation on Disease Data

The DRIVE, CHASE_DB1, and STARE datasets, each comprising only 10 to 20 images, provide a limited data volume in which the efficacy of our method has been substantiated. Nonetheless, the advent of larger and more complex datasets necessitates a reevaluation of our methodology. This necessity led us to test our approach on the FIVES dataset, which includes 800 images, evenly distributed among diabetic retinopathy (DR), age-related macular degeneration (AMD), glaucoma (GC), and normal vision categories, allowing for disease-specific assessments. Results from Table 4 reveal that our KaLDeX model excels across several metrics on the FIVES dataset. Furthermore, the FIVES dataset’s annotations were made directly on the images by trained experts without supplementary equipment, ensuring that the annotated vessels are readily visible. This aspect ostensibly simplifies the learning process for neural networks. Therefore, it can be seen from the table that, due to the distinct vascular structures, different methods can achieve relatively high accuracy.

4.2.3. Structural Continuity Preservation

To evaluate our method’s ability to preserve the overall continuity of vascular structures, we use the Centerline Dice (cLDICE) metric to assess the topological continuity of tubular structures. In Table 5, we can see that our method consistently outperforms others in maintaining vascular continuity across all experimental datasets. This superior performance indicates that KaLDeX is more effective in maintaining the overall continuity of vascular structures, which is essential for reliable medical

image analysis. In the ablation study section, we will further discuss the impact of our model on vascular continuity and the effect of the adopted topological loss function on continuity.

4.2.4. One-shot Training and Few-shot Training

Based on both qualitative and quantitative analyses across various datasets, the effectiveness of vascular segmentation is demonstrably excellent. Evaluations on the FIVES dataset reveal that when sufficient data volume and clear image annotations are available, the performance of different models is notably high with minimal differences. However, in the medical imaging domain, patient data is subject to privacy protections, resulting in very limited publicly available data. Furthermore, pixel-level vascular annotation is an exceedingly difficult and time-consuming task, requiring approximately 3–5 hours per image. Consequently, data volumes for retinal vascular segmentation topics are particularly sparse.

To further explore the efficacy of our method trained on limited datasets, we examined our model’s capability by reducing training samples. In accordance with the partitioning method applied to the dataset in Section 4.1.1, DRIVE, CHASE_DB1, and STARE have 20, 20, and 15 images in training sets, respectively, while the training sets for OCTA_3mm, OCTA_6mm, FIVES_AMD, FIVES_DR, FIVES_GC, and FIVES_Normal consist of 250, 150, 150, 150, 150, and 150 images, respectively. We evaluated our model’s performance on minimal data by reducing training set sizes and then testing on the entire test set, setting the number of training samples in DRIVE, CHASE_DB1, and STARE to 1, 5, 10, and ALL, and in OCTA and FIVES to 1, 10, 50, and ALL.

Table 1: Comparison with the State-of-The-Art Methods On DRIVE and CHASE_DB1

Methods	Year	DRIVE (%)						CHASE_DB1 (%)					
		Acc	Sen	Spe	AUC	Dice	IOU	Acc	Sen	Spe	AUC	Dice	IOU
U-Net	2015	96.78	80.57	98.33	98.25	81.41	68.64	97.43	76.50	98.84	98.36	78.98	65.26
UNet++	2018	96.79	78.91	98.50	98.25	81.14	68.27	97.39	83.57	98.32	98.81	80.15	66.88
DUNet	2019	96.81	81.07	98.45	98.17	81.07	68.17	97.26	80.69	98.36	98.33	79.02	65.32
TransUNet	2021	96.62	79.06	98.31	97.74	80.39	67.21	97.30	83.84	98.20	98.48	79.64	66.17
FR-UNet	2022	97.05	83.56	98.37	98.89	83.16	71.20	97.48	87.98	98.14	99.13	81.51	68.82
SwinUNETRV2	2023	96.98	79.83	98.38	97.86	79.96	66.61	97.46	82.83	98.38	98.76	79.37	65.80
PVT-GCASCADe	2023	96.89	83.00	98.22	–	82.10	69.70	97.71	85.84	98.51	–	82.51	70.24
KaLDeX(ours)	2024	97.25	83.40	98.54	98.92	83.75	72.05	97.77	82.46	98.83	99.11	82.78	70.62

Table 2: Quantification results on STARE

Methods	Year	STARE (%)					
		Acc	Sen	Spe	AUC	Dice	IOU
U-Net	2015	97.30	78.50	98.84	98.75	81.18	68.56
UNet++	2018	96.34	70.09	98.83	98.84	81.50	69.02
DUNet	2019	97.19	77.57	98.93	99.03	82.78	69.38
TransUNet	2021	97.27	77.87	98.98	98.99	81.06	69.97
FR-UNet	2022	97.52	83.27	98.69	99.14	83.30	71.56
KaLDeX(ours)	2024	97.85	80.72	99.10	99.01	83.62	71.85

Table 3: Quantification results on OCTA

Methods	Year	OCTA_3mm (%)		OCTA_6mm (%)	
		Acc	Dice	Acc	Dice
U-Net	2015	95.45	88.35	95.21	85.03
U-Net++	2018	95.98	88.64	95.73	85.67
DUNet	2019	97.52	88.22	96.73	87.70
TransUNet	2021	96.32	90.89	97.42	88.67
FR-UNet	2022	98.84	91.15	98.02	88.85
KaLDeX(ours)	2024	98.89	91.59	98.21	89.13

Fig. 7 showcases the visualization of test results on DRIVE and OCTA_3mm using training sample sizes of 1, 5, 10, ALL, and 1, 10, 50, ALL, respectively. It is clear that even with a single sample for training, our model can still delineate distinct vascular structures, albeit with slightly poorer segmentation in smaller vessel areas.

4.2.5. Cross Evaluation Study

Although our model exhibits exceptional performance on both datasets with substantial and extremely limited data volumes, the quality of a model should also consider its ability to generalize beyond the distribution of the training dataset. To assess the generalizability and robustness of our proposed method, we conducted cross-training experiments. In these experiments, a model trained to convergence on dataset A was applied to dataset B to test its performance. Specifically, we first

trained models separately on DRIVE, CHASE_DB1, STARE, OCTA_3mm, and OCTA_6mm. Then, we tested the trained models on datasets they were not trained on. Given the distinct data types of fundus images and OCTA, we also introduced a model jointly trained on DRIVE and OCTA_3mm. In Table 6, we reported on metrics such as ACC (Accuracy), AUC (Area Under the Curve), and DICE. Generally, the results of testing models trained across different data distributions are not as good as those trained on original datasets, hence the best results are located on the diagonal of the table. The performance of models trained on fundus images and then tested on other fundus datasets significantly surpasses that of models trained on OCTA and tested on fundus images, and vice versa. The model trained on the combined DRIVE and OCTA_3mm dataset and tested across various datasets performed exceptionally well. Compared to previous quantitative results, our cross-evaluation outcomes are comparable to those achieved by UNet++ trained directly on the original datasets.

4.2.6. Ablation Study

To investigate the efficacy of each proposed module within our study, we conducted ablation experiments on each submodule, with the results presented in Table 7. Our ablation studies evaluated the impact of the proposed LD module and the CA module and the topology loss (\mathcal{L}_{ossp}) used in fine-tune phase. Notably, the inclusion of the linear deformable module resulted in a significant enhancement in segmentation performance (Acc, Dice), especially on the OCTA dataset, where the addition of the linear deformable module alone nearly improved Acc and Dice by 2%. The CA module and topological loss are greatly beneficial in improving the continuity of the overall vascular structure. On average, the CA module improved the cDice metric by 1.5% across different datasets, while the topological loss improved the cDice metric by 2% on average. From the ablation experiment results, it is evident that our LD module significantly enhances the accuracy of vascular segmentation. Since the accuracy of main vessel segmentation is already very high in current models, the improvement in accuracy is largely due to better recognition of small vessels. We also visualized the receptive field of our linear deformable con-

Table 4: Quantification results on FIVES

Methods	Year	AMD (%)			DR(%)			GC (%)			Normal(%)		
		Acc	AUC	DICE	Acc	AUC	DICE	Acc	AUC	DICE	Acc	AUC	DICE
U-Net	2015	98.43	97.84	90.33	98.45	97.47	88.46	97.88	96.89	85.35	98.30	97.76	88.64
UNet++	2018	98.42	98.38	90.75	98.25	97.85	88.83	98.06	98.02	86.45	98.37	98.15	90.36
TransUNet	2021	98.72	98.06	92.31	98.84	98.39	90.41	99.06	98.84	87.42	98.52	98.64	91.09
FR-UNet	2022	98.83	99.08	91.98	98.81	99.26	90.18	98.87	99.12	87.14	98.48	99.19	90.82
KaLDeX(ours)	2024	98.93	99.32	92.43	98.83	99.28	90.38	99.04	99.18	87.46	98.53	99.22	91.13

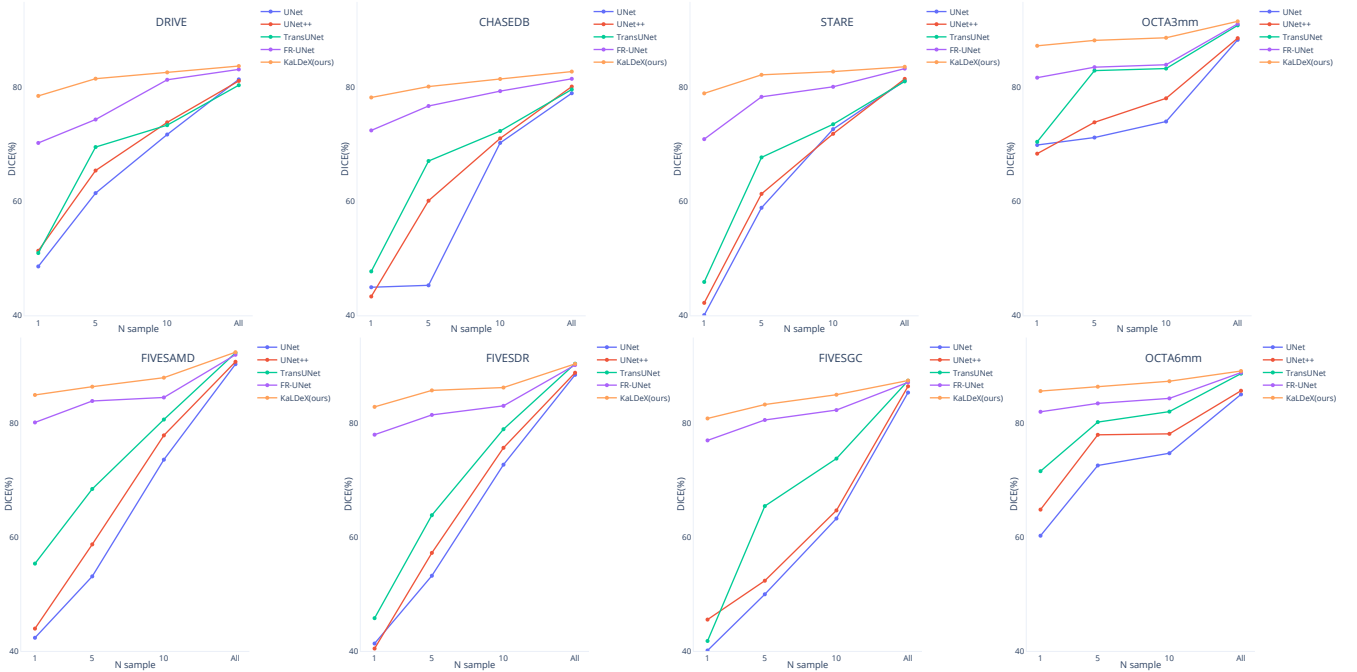


Figure 7: The results of testing on multiple datasets using different numbers of training samples

Table 5: Quantify Structural Continuity Preservation using the cIDice metric

Methods	DRIVE (%)	FIVES (%)	STARE (%)	CHASE DBI(%)	OCTA 3mm(%)	OCTA 6mm(%)
U-Net	75.71	83.78	80.99	78.92	86.98	86.74
UNet++	76.93	85.31	81.54	81.75	88.35	87.91
DUNet	76.33	84.97	82.02	81.62	89.30	87.14
TransUNet	77.67	85.65	82.31	81.31	89.56	87.98
FR-UNet	82.39	88.25	84.46	84.20	92.98	90.57
KaLDeX(ours)	83.03	89.61	86.61	85.14	94.02	92.18

volution in Fig. 8, which shows that our LD module provides a tighter fit to the vascular structure. The results of the continuity-preserving metric cIDice indicate that the CA module, through cross-attention, enhances the network’s recognition of the overall vascular structure by aggregating global and local features. Additionally, the topological loss greatly improves the continuity of the vasculature by fine-tuning the segmentation results.

5. Discussion

This paper presents a network architecture and an optimized topological loss function that significantly enhance the accuracy of ophthalmic image segmentation. In the experiments section, we explore the performance of the proposed network architecture in segmenting blood vessels across various types of ophthalmic images. The results indicate that our method surpasses the current state-of-the-art (SOTA) methods in terms of segmentation accuracy for both fundus and OCTA images. Moreover, on a larger dataset, FIVES, under the influence of multiple diseases, our method still achieves remarkably high segmentation accuracy. In the experimental section, we validate our model’s capability for few-shot learning by reducing the number of training samples, which is feasible because segmenting images in patches enables the network to learn a more extensive data distribution from a limited dataset. We also confirm our model’s generalizability through cross-evaluation, training on dataset A, and assessment on dataset B. The experimental results validate the generalization capability, demonstrating that the model has learned to identify tubular structures, primarily

Table 6: Quantitative evaluation results of model generalization using cross evaluation.

Training	Models	DRIVE(%)			CHASE_DB1(%)			STARE(%)			OCTA_3mm(%)		OCTA_6mm(%)	
		Acc	AUC	Dice	Acc	AUC	Dice	Acc	AUC	Dice	Acc	Dice	Acc	Dice
DRIVE	UNet	96.78	98.25	81.41	93.03	82.19	67.20	95.08	89.26	61.12	86.05	40.26	85.37	48.65
	KaLDeX	97.25	98.92	83.75	95.64	97.04	78.89	96.47	96.94	75.35	93.37	62.12	92.76	65.83
OCTA_3mm	UNet	89.99	57.78	21.78	87.42	40.77	32.31	86.05	54.99	28.62	95.45	88.35	94.77	83.96
	KaLDeX	93.04	87.26	64.34	91.53	86.58	65.66	92.49	88.47	65.50	98.89	91.59	97.83	88.86
DRIVE+OCTA_3mm	UNet	96.69	97.49	81.03	93.05	81.10	67.31	95.35	88.79	61.27	95.51	88.47	94.91	84.17
	KaLDeX	97.25	98.87	83.47	95.60	96.89	78.87	96.47	96.87	75.11	98.79	91.56	98.07	89.12

Table 7: Ablation study of the proposed LDCA module

Methods	DRIVE (%)			CHASE_DB1 (%)			STARE (%)			OCTA_3mm (%)			OCTA_6mm (%)		
	Acc	Dice	cIDice	Acc	Dice	cIDice	Acc	Dice	cIDice	Acc	Dice	cIDice	Acc	Dice	cIDice
Baseline	96.79	81.40	76.93	97.41	80.42	81.75	97.34	81.59	81.54	96.18	88.67	88.35	96.32	85.81	87.91
Baseline+LD	97.14	82.65	77.31	97.58	81.53	81.98	97.55	81.74	83.01	98.12	91.04	89.87	98.02	88.05	88.94
Baseline+LDCA	97.20	82.71	80.17	97.69	81.61	83.33	97.70	81.87	84.65	98.88	91.45	92.07	98.12	88.85	90.91
Baseline+LDCA+ \mathcal{L}_{ossp}	97.25	82.87	83.03	97.77	81.72	85.14	97.85	82.20	86.61	98.89	91.59	94.02	98.21	89.13	92.18

through the LD module in our model. In terms of preserving vascular continuity, we assess the overall effectiveness of the model and separately analyze the impact of different network modules and topological loss on vascular continuity in the ablation study section.

We also investigate issues inherent in the data itself throughout experiments. In DRIVE dataset, for small vessel regions, without the aid of additional equipment, there is a significant discrepancy in annotations between the experts. Expert 2’s annotations visually align more closely with the understanding of vascular structures. However, as the existing research relies on Expert 1’s labels, the quantified results in this paper are tested on Expert 1’s annotations. We also quantitatively assess the annotations of Expert 2, our method achieves an AUC of 99.99 and an ACC of 98.89. This data underscores the importance of diverse label information in enhancing quantitative results. Therefore, in future research on ophthalmic image vascular segmentation, more detailed annotations of vascular structures, or the use of more precise equipment for auxiliary annotation to provide high-quality ground truth, are equally crucial for improving the performance of network models.

6. Conclusions

In this paper, we propose a novel network KaLDeX, leveraging Kalman based linear deformable cross attention mechanism to improve the segmentation accuracy of vascular structures in ophthalmic images. By combining a Kalman filter-based linear deformable convolution module with cross-attention, our approach refines the focus on vascular regions and enhances the discernment of small vascular structures. Integrated within the UNet++ framework, the LDCA module successfully merges detailed features with broad contextual information, facilitating a comprehensive understanding of the vascular network. The proposed method in this paper brings innovative advancements

to the field of medical image analysis by enhancing the segmentation accuracy of vascular structures in ophthalmic images.

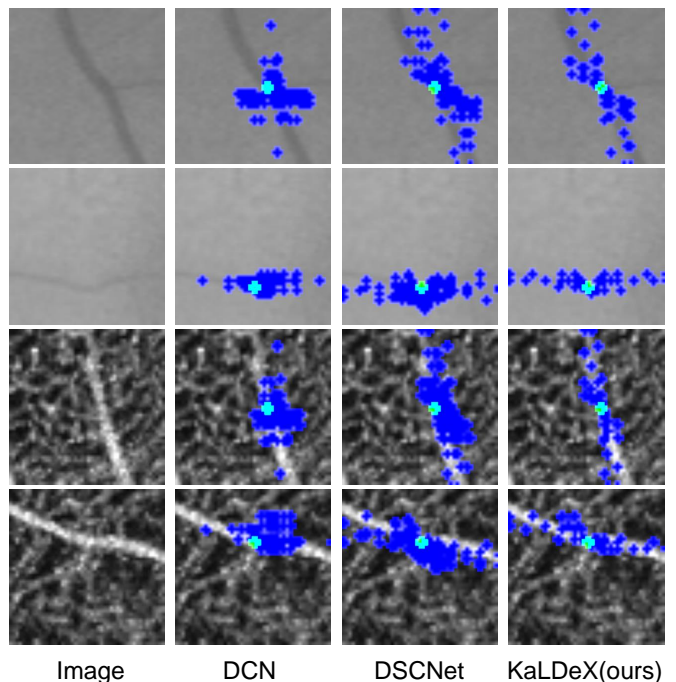


Figure 8: The first and second rows show fundus images, highlighting the convolutional fields of view for horizontal and vertical vascular structures across different deformable convolution. The third and fourth rows present the visualized fields of view for deformable convolution applied to OCTA images.

Data declaration

Data underlying the results presented in this paper are available in DRIVE [55], STARE[57], CHASE_DB1 [56], FIVES [58] and OCTA-500 [59].

Declaration of competing interest

The authors declare that they have no known competing financial interests or personal relationships that could have appeared to influence the work reported in this paper.

Acknowledgments

This work is supported by Bavarian research alliance, Germany (AZ-1503-21).

References

- [1] S. You, E. Bas, D. Erdogmus, J. Kalpathy-Cramer, Principal curved based retinal vessel segmentation towards diagnosis of retinal diseases, in: 2011 IEEE First International Conference on Healthcare Informatics, Imaging and Systems Biology, IEEE, 2011, pp. 331–337.
- [2] Y. Zhao, Z. Zhao, J. Yang, L. Li, M. A. Nasser, D. Zapp, Ai-based fully automatic analysis of retinal vascular morphology in pediatric high myopia, *BMC ophthalmology* 24 (1) (2024) 415.
- [3] C. D. REGAN, C. S. FOSTER, Retinal vascular diseases: clinical presentation and diagnosis, *International Ophthalmology Clinics* 26 (2) (1986) 25–53.
- [4] Z. Zhao, S. Faghiroohi, J. Yang, K. Huang, N. Navab, M. Maier, M. A. Nasser, Unobtrusive biometric data de-identification of fundus images using latent space disentanglement, *Biomedical Optics Express* 14 (10) (2023) 5466–5483.
- [5] T. H. Rim, A. W. J. Teo, H. H. S. Yang, C. Y. Cheung, T. Y. Wong, Retinal vascular signs and cerebrovascular diseases, *Journal of Neuro-ophthalmology* 40 (1) (2020) 44–59.
- [6] E. Uysal, G. E. Güraksin, Computer-aided retinal vessel segmentation in retinal images: convolutional neural networks, *Multimedia Tools and Applications* 80 (2021) 3505–3528.
- [7] Q. Qin, Y. Chen, A review of retinal vessel segmentation for fundus image analysis, *Engineering Applications of Artificial Intelligence* 128 (2024) 107454.
- [8] C. Chen, J. H. Chuah, R. Ali, Y. Wang, Retinal vessel segmentation using deep learning: a review, *IEEE Access* 9 (2021) 111985–112004.
- [9] Z. Zhao, Y. Zhao, J. Yang, K. Huang, N. Navab, M. A. Nasser, Kldd: Kalman filter based linear deformable diffusion model in retinal image segmentation, *arXiv preprint arXiv:2410.02808* (2024).
- [10] J. V. Soares, J. J. Leandro, R. M. Cesar, H. F. Jelinek, M. J. Cree, Retinal vessel segmentation using the 2-d gabor wavelet and supervised classification, *IEEE Transactions on Medical Imaging* 25 (9) (2006) 1214–1222.
- [11] Z. Zhao, J. Yang, S. Faghiroohi, K. Huang, M. Maier, N. Navab, M. A. Nasser, Label-preserving data augmentation in latent space for diabetic retinopathy recognition, in: *International Conference on Medical Image Computing and Computer-Assisted Intervention*, Springer, 2023, pp. 284–294.
- [12] X. Li, Y. Jiang, M. Li, S. Yin, Lightweight attention convolutional neural network for retinal vessel image segmentation, *IEEE Transactions on Industrial Informatics* 17 (3) (2020) 1958–1967.
- [13] O. Ronneberger, P. Fischer, T. Brox, U-net: Convolutional networks for biomedical image segmentation, in: *Medical Image Computing and Computer-Assisted Intervention—MICCAI 2015: 18th International Conference, Munich, Germany, October 5–9, 2015, Proceedings, Part III* 18, Springer, 2015, pp. 234–241.
- [14] J. Hu, H. Wang, S. Gao, M. Bao, T. Liu, Y. Wang, J. Zhang, S-unet: A bridge-style u-net framework with a saliency mechanism for retinal vessel segmentation, *IEEE Access* 7 (2019) 174167–174177.
- [15] Z. Zhou, M. M. Rahman Siddiquee, N. Tajbakhsh, J. Liang, Unet++: A nested u-net architecture for medical image segmentation, in: *Deep Learning in Medical Image Analysis and Multimodal Learning for Clinical Decision Support: 4th International Workshop, DLMIA 2018, and 8th International Workshop, ML-CDS 2018, Held in Conjunction with MICCAI 2018, Granada, Spain, September 20, 2018, Proceedings 4*, Springer, 2018, pp. 3–11.
- [16] X. Li, W. Qian, D. Xu, C. Liu, Image segmentation based on improved unet, in: *Journal of Physics: Conference Series*, Vol. 1815, IOP Publishing, 2021, p. 012018.
- [17] D. Hirahara, E. Takaya, M. Kadowaki, Y. Kobayashi, T. Ueda, Effect of the pixel interpolation method for downsampling medical images on deep learning accuracy, *Journal of Computer and Communications* 9 (11) (2021) 150–156.
- [18] J. Dai, H. Qi, Y. Xiong, Y. Li, G. Zhang, H. Hu, Y. Wei, Deformable convolutional networks, in: *Proceedings of the IEEE international conference on computer vision*, 2017, pp. 764–773.
- [19] Q. Jin, Z. Meng, T. D. Pham, Q. Chen, L. Wei, R. Su, Dunet: A deformable network for retinal vessel segmentation, *Knowledge-Based Systems* 178 (2019) 149–162.
- [20] Y. Qi, Y. He, X. Qi, Y. Zhang, G. Yang, Dynamic snake convolution based on topological geometric constraints for tubular structure segmentation, in: *Proceedings of the IEEE/CVF International Conference on Computer Vision*, 2023, pp. 6070–6079.
- [21] S. Shit, J. C. Paetzold, A. Sekuboyina, I. Ezhov, A. Unger, A. Zhyhka, J. P. Plum, U. Bauer, B. H. Menze, cldice—a novel topology-preserving loss function for tubular structure segmentation, in: *Proceedings of the IEEE/CVF conference on computer vision and pattern recognition*, 2021, pp. 16560–16569.
- [22] J. R. Clough, N. Byrne, I. Oksuz, V. A. Zimmer, J. A. Schnabel, A. P. King, A topological loss function for deep-learning based image segmentation using persistent homology, *IEEE transactions on pattern analysis and machine intelligence* 44 (12) (2020) 8766–8778.
- [23] J. Cervantes, J. Cervantes, F. García-Lamont, A. Yee-Rendon, J. E. Cabrera, L. D. Jalili, A comprehensive survey on segmentation techniques for retinal vessel segmentation, *Neurocomputing* 556 (2023) 126626.
- [24] S. Y. Shin, S. Lee, I. D. Yun, K. M. Lee, Deep vessel segmentation by learning graphical connectivity, *Medical image analysis* 58 (2019) 101556.
- [25] N. Siddique, S. Paheding, C. P. Elkin, V. Devabhaktuni, U-net and its variants for medical image segmentation: A review of theory and applications, *Ieee Access* 9 (2021) 82031–82057.
- [26] T. A. Soomro, A. J. Afifi, L. Zheng, S. Soomro, J. Gao, O. Hellwich, M. Paul, Deep learning models for retinal blood vessels segmentation: a review, *IEEE Access* 7 (2019) 71696–71717.
- [27] N. Wang, K. Li, G. Zhang, Z. Zhu, P. Wang, Improvement of retinal vessel segmentation method based on u-net, *Electronics* 12 (2) (2023) 262.
- [28] F. I. Diakogiannis, F. Waldner, P. Caccetta, C. Wu, Resunet-a: A deep learning framework for semantic segmentation of remotely sensed data, *ISPRS Journal of Photogrammetry and Remote Sensing* 162 (2020) 94–114.
- [29] D. Mahapatra, A. Poellinger, M. Reyes, Interpretability-guided inductive bias for deep learning based medical image, *Medical image analysis* 81 (2022) 102551.
- [30] P. K. Gadosey, Y. Li, E. A. Agyekum, T. Zhang, Z. Liu, P. T. Yamak, F. Essaf, Sd-unet: Stripping down u-net for segmentation of biomedical images on platforms with low computational budgets, *Diagnostics* 10 (2) (2020) 110.
- [31] J. Ba, B. Frey, Adaptive dropout for training deep neural networks, *Advances in neural information processing systems* 26 (2013).
- [32] W. Liu, H. Yang, T. Tian, Z. Cao, X. Pan, W. Xu, Y. Jin, F. Gao, Full-resolution network and dual-threshold iteration for retinal vessel and coronary angiograph segmentation, *IEEE Journal of Biomedical and Health Informatics* 26 (9) (2022) 4623–4634.
- [33] N. Shen, Z. Wang, J. Li, H. Gao, W. Lu, P. Hu, L. Feng, Multi-organ segmentation network for abdominal ct images based on spatial attention and deformable convolution, *Expert Systems with Applications* 211 (2023) 118625.
- [34] S. Dong, Z. Pan, Y. Fu, Q. Yang, Y. Gao, T. Yu, Y. Shi, C. Zhuo, Deu-net 2.0: Enhanced deformable u-net for 3d cardiac cine mri segmentation, *Medical Image Analysis* 78 (2022) 102389.
- [35] G. Tsechpenakis, Deformable model-based medical image segmentation, in: *Multi Modality State-of-the-Art Medical Image Segmentation and Registration Methodologies: Volume 1*, Springer, 2011, pp. 33–67.
- [36] X. Yang, Z. Li, Y. Guo, D. Zhou, Dcu-net: A deformable convolutional neural network based on cascade u-net for retinal vessel segmentation, *Multimedia Tools and Applications* 81 (11) (2022) 15593–15607.
- [37] A. Vaswani, N. Shazeer, N. Parmar, J. Uszkoreit, L. Jones, A. N. Gomez,

- L. Kaiser, I. Polosukhin, Attention is all you need, *Advances in neural information processing systems* 30 (2017).
- [38] R. Hou, H. Chang, B. Ma, S. Shan, X. Chen, Cross attention network for few-shot classification, *Advances in neural information processing systems* 32 (2019).
- [39] Y. Yuan, L. Zhang, L. Wang, H. Huang, Multi-level attention network for retinal vessel segmentation, *IEEE Journal of Biomedical and Health Informatics* 26 (1) (2021) 312–323.
- [40] Y. Lv, H. Ma, J. Li, S. Liu, Attention guided u-net with atrous convolution for accurate retinal vessels segmentation, *IEEE Access* 8 (2020) 32826–32839.
- [41] C. Dong, S. Xu, D. Dai, Y. Zhang, C. Zhang, Z. Li, A novel multi-attention, multi-scale 3d deep network for coronary artery segmentation, *Medical Image Analysis* 85 (2023) 102745.
- [42] N. Mu, Z. Lyu, M. Rezaeitaleshmahalleh, J. Tang, J. Jiang, An attention residual u-net with differential preprocessing and geometric post-processing: Learning how to segment vasculature including intracranial aneurysms, *Medical image analysis* 84 (2023) 102697.
- [43] J. Cheng, S. Tian, L. Yu, C. Gao, X. Kang, X. Ma, W. Wu, S. Liu, H. Lu, Resganet: Residual group attention network for medical image classification and segmentation, *Medical Image Analysis* 76 (2022) 102313.
- [44] L. Xia, H. Zhang, Y. Wu, R. Song, Y. Ma, L. Mou, J. Liu, Y. Xie, M. Ma, Y. Zhao, 3d vessel-like structure segmentation in medical images by an edge-reinforced network, *Medical Image Analysis* 82 (2022) 102581.
- [45] M. R. K. Mookiah, S. Hogg, T. J. MacGillivray, V. Prathiba, R. Pradeepa, V. Mohan, R. M. Anjana, A. S. Doney, C. N. Palmer, E. Trucco, A review of machine learning methods for retinal blood vessel segmentation and artery/vein classification, *Medical Image Analysis* 68 (2021) 101905.
- [46] C. Guo, M. Szemenyei, Y. Yi, W. Wang, B. Chen, C. Fan, Sa-unet: Spatial attention u-net for retinal vessel segmentation, in: *2020 25th international conference on pattern recognition (ICPR)*, IEEE, 2021, pp. 1236–1242.
- [47] Y.-f. Zhu, X. Xu, X.-d. Zhang, M.-s. Jiang, Ccs-unet: a cross-channel spatial attention model for accurate retinal vessel segmentation, *Biomedical Optics Express* 14 (9) (2023) 4739–4758.
- [48] E. Pahwa, D. Mehta, S. Kapadia, D. Jain, A. Luthra, Medskip: Medical report generation using skip connections and integrated attention, in: *Proceedings of the IEEE/CVF International Conference on Computer Vision*, 2021, pp. 3409–3415.
- [49] A. Agarwal, C. Arora, Attention attention everywhere: Monocular depth prediction with skip attention, in: *Proceedings of the IEEE/CVF Winter Conference on Applications of Computer Vision*, 2023, pp. 5861–5870.
- [50] X. Mao, Y. Zhao, B. Chen, Y. Ma, Z. Gu, S. Gu, J. Yang, J. Cheng, J. Liu, Deep learning with skip connection attention for choroid layer segmentation in oct images, in: *2020 42nd Annual International Conference of the IEEE Engineering in Medicine & Biology Society (EMBC)*, IEEE, 2020, pp. 1641–1645.
- [51] G. Welch, G. Bishop, et al., An introduction to the kalman filter (1995).
- [52] C.-C. Wong, C.-M. Vong, Persistent homology based graph convolution network for fine-grained 3d shape segmentation, in: *Proceedings of the IEEE/CVF International Conference on Computer Vision*, 2021, pp. 7098–7107.
- [53] L. Wasserman, Topological data analysis, *Annual Review of Statistics and Its Application* 5 (2018) 501–532.
- [54] R. Brüel-Gabrielsson, B. J. Nelson, A. Dwaraknath, P. Skraba, L. J. Guibas, G. Carlsson, A topology layer for machine learning (2020). [arXiv:1905.12200](https://arxiv.org/abs/1905.12200).
- [55] J. Staal, M. D. Abràmoff, M. Niemeijer, M. A. Viergever, B. Van Ginneken, Ridge-based vessel segmentation in color images of the retina, *IEEE transactions on medical imaging* 23 (4) (2004) 501–509.
- [56] K. U. Research., Chase.db1 database, [EB/OL], <http://blogs.kingston.ac.uk/retinal/chasedb1/> Accessed Jan. 2011.
- [57] A. Hoover, V. Kouznetsova, M. Goldbaum, Locating blood vessels in retinal images by piecewise threshold probing of a matched filter response, *IEEE Transactions on Medical Imaging* 19 (3) (2000) 203–210.
- [58] K. Jin, X. Huang, J. Zhou, Y. Li, Y. Yan, Y. Sun, Q. Zhang, Y. Wang, J. Ye, Fives: A fundus image dataset for artificial intelligence based vessel segmentation, *Scientific Data* 9 (1) (2022) 475.
- [59] M. Li, K. Huang, Q. Xu, J. Yang, Y. Zhang, K. Xie, S. Yuan, Q. Liu, Q. Chen, Octa-500: a retinal dataset for optical coherence tomography angiography study, *Medical Image Analysis* (2024) 103092.
- [60] M. M. Rahman, R. Marculescu, G-cascade: Efficient cascaded graph convolutional decoding for 2d medical image segmentation, in: *Proceedings of the IEEE/CVF Winter Conference on Applications of Computer Vision*, 2024, pp. 7728–7737.
- [61] Y. He, V. Nath, D. Yang, Y. Tang, A. Myronenko, D. Xu, Swinunetr-v2: Stronger swin transformers with stagewise convolutions for 3d medical image segmentation, in: *International Conference on Medical Image Computing and Computer-Assisted Intervention*, Springer, 2023, pp. 416–426.
- [62] W. Wang, J. Zhong, H. Wu, Z. Wen, J. Qin, Rvseg-net: An efficient feature pyramid cascade network for retinal vessel segmentation, in: *Medical Image Computing and Computer Assisted Intervention–MICCAI 2020: 23rd International Conference, Lima, Peru, October 4–8, 2020, Proceedings, Part V 23*, Springer, 2020, pp. 796–805.